Check for updates

Multiscale modelling of the radical-induced chemistry of acetohydroxamic acid in aqueous solution†

Jacy K. Conrad, [ID] *[a] Corey D. Pilgrim, [ID] [a] Simon M. Pimblott, [ID] [a] Stephen P. Mezyk [ID] [b] and Gregory P. Horne [ID] *[a]

Acetohydroxamic acid (AHA) is a small organic acid with a wide variety of industrial, biological, and pharmacological applications. A deep fundamental molecular level understanding of the mechanisms responsible for the radical-induced reactions of AHA in these environments is necessary to predict and control their behaviour and elucidate their interplay with other attendant chemical species, for example, the oxidative degradation products of AHA. To this end, we present a comprehensive, multiscale computer model for interrogating the radical-induced degradation of AHA in acidic aqueous solutions. Model predictions were critically evaluated by a systematic experimental radiation chemistry investigation, leveraging time-resolved electron pulse irradiation techniques for the measurement of new radical reaction rate coefficients, and steady-state gamma irradiations for the identification and quantification of AHA degradation products: acetic acid, hydroxylamine, nitrous oxide, and molecular hydrogen, with formic acid and methane as minor products. Excellent agreement was achieved between calculation and experiment, indicating that this fundamental model can accurately predict the degradation pathways of AHA under irradiation in acidic aqueous solutions.

Introduction

Hydroxamic acids have distinct chemical properties that have been extensively leveraged for industrial, biological, and pharmacological applications.[1–3] For example, due to its strong bidentate metal chelating properties,[4] acetohydroxamic acid (AHA, $CH_3CONHOH$) has been proposed for use in used nuclear fuel reprocessing technologies for the reduction and complexation of plutonium and neptunium ions.[5–8] AHA is also used as an oral drug to treat struvite kidney stones,[9] urinary tract infections,[10] metal poisoning,[11] and to complex metalloenzymes related to cancer progression.[1,12,13] In addition, hydroxamic acids are prevalent in creating new pharmaceuticals *via* the promising strategy of linked hybrid bioactive fragments.[14–16] In each of these applications, the stability of AHA is an important consideration. Hydroxamic acids are subject to degradation *via* hydrolysis under acidic conditions. The hydrolysis of AHA yields

acetic acid (CH_3COOH) and hydroxylamine (HA, NH_3OH^+) products:[17–19]

$$CH_3CONHOH + H_3O^+ \rightarrow CH_3COOH + NH_3OH^+,$$
$$k_1 = 3.92 \times 10^{-5} \text{ M}^{-1} \text{ s}^{-1}. \quad (1)$$
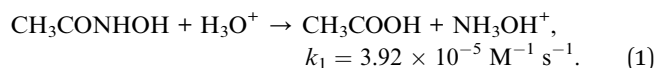
AHA will also interact with radiolysis products arising from the intense, multi-component, radiation fields present in used nuclear fuel reprocessing solvent systems, and with free radical species generated in the human body. Further, the oxidative decomposition of hydroxamic acids is important for considerations in wastewater treatment, either by the use of polyhydroxamic acids as metal chelators and flocculating agents for treatment,[20] or for its disposal *via* advanced oxidation processes (AOPs), many of which leverage hydroxyl radical (·OH) and/or hydrogen peroxide (H_2O_2) mediated chemistry to promote complete mineralization of organic contaminants.[21–26]

Consequently, a quantitative understanding of these hydroxamic acid oxidation and reduction processes at a fundamental molecular level is necessary to facilitate their prediction and control in various macroscopic systems and processes. This complete level of mechanistic understanding can readily be attained by utilizing radiation chemistry, a powerful means for directly characterizing the redox behavior of various transient and steady-state radicals, ions, and molecules. For aqueous solutions, the radiolysis of water produces a suite of primary
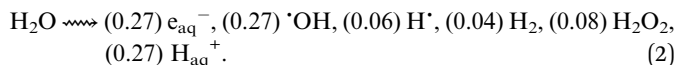
[a]Center for Radiation Chemistry Research, Idaho National Laboratory, 1955 N. Fremont Ave., Idaho Falls, ID, 83415, USA. E-mail: jacy.conrad@inl.gov; gregory. horne@inl.gov

[b]Department of Chemistry and Biochemistry, California State University Long Beach, 1250 Bellflower Blvd., Long Beach, CA, 90840, USA

† Electronic supplementary information (ESI) available: Chemicals, analytical techniques and calibration curves, experimental and computational methodologies, escape yields calculated from stochastic model, kinetic chemical reaction set used, and rate coefficients determined in this work. See DOI: https://doi.org/10.1039/d2ra03392e
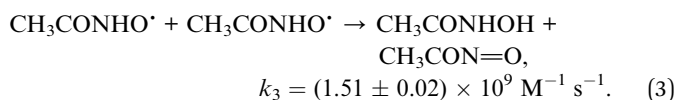
radiolysis products, many of which are redox active (*i.e.*, e_{aq}^-, $H^{\bullet}$, $^{\bullet}OH$, and H_2O_2):[27]

$$H_2O \rightsquigarrow (0.27) e_{aq}^-, (0.27) \,^{\bullet}OH, (0.06) H^{\bullet}, (0.04) H_2, (0.08) H_2O_2, \\ (0.27) H_{aq}^+. \quad (2)$$

Here the numbers in parentheses are the radiation chemical yields for pure water,[28] known commonly as *G*-values, in units of $\mu mol \, J^{-1}$.[29] The reactive species from water radiolysis can undergo subsequent reactions with many of the water matrix chemicals present to generate secondary radiolysis products, for example, the reduction of oxygen ($O_2 + e_{aq}^-$) to form superoxide ($O_2^{\bullet -}$).[27] Both the primary and secondary radiolysis species have the potential to drive chemical changes in AHA.

There have been a few studies that characterized the overall products from the gamma irradiation of AHA in concentrated nitric acid solutions for applications in used nuclear fuel reprocessing, but these works did not attempt to determine specific reaction mechanisms.[30,31] In addition to those, Samuni and Goldstein measured second-order rate coefficients (*k*) for the reactions of AHA with $^{\bullet}OH$, $^{\bullet}CO_3^-$, azide ($^{\bullet}N_3$), and nitrite ($NO_2^{\bullet}$) radicals using time-resolved electron pulse radiolysis techniques to show that the product of these radical-induced AHA one-electron oxidations was always a nitroxide radical, $CH_3CONHO^{\bullet}$, and that no reaction occurs between AHA and the $O_2^{\bullet -}$ radical.[32] The structure of the nitroxide radical has been established using electron paramagnetic resonance (EPR) methods.[33,34] A mechanism was proposed for the disproportionation of the transient nitroxide radical to form AHA and an unstable acyl nitroso intermediate ($CH_3CON{=}O$):[32]

$$CH_3CONHO^{\bullet} + CH_3CONHO^{\bullet} \rightarrow CH_3CONHOH + \\ CH_3CON{=}O, \\ k_3 = (1.51 \pm 0.02) \times 10^9 \, M^{-1} \, s^{-1}. \quad (3)$$

Beyond these works, there is little mechanistic understanding of the aqueous radical-induced oxidation of AHA, and no studies of the complementary mechanisms for its radical-induced reduction chemistry.

To this end we present a new, comprehensive, multiscale computer model for the prediction of the free radical-induced mechanistic behavior of AHA in acidic aqueous solutions. The approach combines a stochastic model of the radiation track structure[35–37] with a deterministic homogeneous bulk chemistry model, both pieces of which are essential to fully represent the system behavior. This model accounts for different solute concentrations, varying radical production rates, and pH, and has been validated and verified by comparison with experimental results from a new systematic study of the steady-state gamma radiolysis of AHA in pure water and aqueous perchloric acid solutions, in which the concentrations of AHA, and its potential final degradation products: acetic acid, HA, nitrite/nitrous acid (NO_2^-/HNO_2), formic acid (HCOOH), molecular hydrogen (H_2), nitrous oxide (N_2O), and methane (CH_4) were analyzed. These data augment the hydrolysis kinetics previously established for AHA,[17–19] providing a complete model for the loss of this acid under different aqueous conditions.

Methods

Chemicals and analytical methods

Details of the chemicals used and the UV-visible spectroscopy, ion chromatography (IC), gas chromatography (GC), and proton nuclear magnetic resonance (^{1}H-NMR) spectroscopy methods are given in the ESI.†

Time-resolved electron pulse radiolysis

Radical reaction kinetics were measured for AHA and HA by transient absorption spectroscopy using the Brookhaven National Laboratory (BNL) picosecond Laser Electron Accelerator Facility (LEAF)[38] and the Notre Dame Radiation Laboratory (NDRL) nanosecond electron pulse linear accelerator facility.[39,40] Dosimetry to determine absolute radical yields per electron pulse was performed using the thiocyanate dosimeter solution ($\lambda_{max} = 470$ nm, using $G^* \, \varepsilon = 5.2 \times 10^{-4} \, m^2 \, J^{-1}$).[41] Isolation and measurement of specific radical species was achieved using the following solution conditions:

• Hydrated electron (e_{aq}^-): direct transient decay kinetics of the e_{aq}^- were observed at 720 nm using N_2- or Ar-saturated aqueous solutions of 0.5 M *t*BuOH at pH 4.0 or 9.8 buffered by 10 mM phosphate with pH adjusted by concentrated $HClO_4$ or NaOH.

• Hydrogen atom ($H^{\bullet}$): the growth kinetics of the *p*CBA radical adduct ($[pCBA{-}H]^{\bullet}$) were monitored at 365 nm in N_2-saturated aqueous solutions containing 100 μM *p*CBA, 20 mM *t*BuOH, and 3.0 M $HClO_4$.

• Hydroxyl radical ($^{\bullet}OH$): competition kinetics with SCN^- were performed by monitoring the $(SCN)_2^{\bullet -}$ transient absorption at 470 nm in N_2O-saturated aqueous solutions using 0.1 mM KSCN at pH 4.0 for protonated AHA, pH 9.8 for deprotonated AHA, and pH 4.0 for HA, buffered by 10 mM phosphate with pH adjusted by concentrated $HClO_4$ or NaOH.

All transient absorption measurements were made using 1 cm optical pathlength quartz cells at ambient room temperature (23–24 °C). Kinetic traces were the average of 8–15 individual measurements. Second-order rate coefficients (*k*) were derived from pseudo-first-order exponential fits (*k'*) to raw kinetic data by plotting *k'* against the reactant concentration weighted by the inverse squares of the experimental uncertainties. Quoted errors for the presented second-order reaction rate coefficients are a combination of measurement precision and sample concentration errors.

Steady-state gamma irradiations

Gamma irradiations were performed on aqueous solutions of 0.50 M AHA with doses up to 100 kGy using the Idaho National Laboratory (INL) Center for Radiation Chemistry Research (CR2) Foss Therapy Services Model 812 Cobalt-60 Gamma Irradiator. The dose rates (Gy min^{-1}) for different positions in the irradiator were determined to be 50–250 Gy min^{-1} using Fricke dosimetry[42] subsequently corrected for the decay of cobalt-60 (^{60}Co, $\tau_{1/2} = 5.27$ years, $E_{\gamma 1} = 1.17$ MeV and $E_{\gamma 2} = 1.33$ MeV) throughout the duration of this study. Solution temperatures were monitored *in situ* during irradiation using a K-type thermocouple and found to be 35–45 °C. Samples for irradiation consisted of aqueous solutions

of 0.50 M AHA in water or in 0.20 M $HClO_4$ sealed in screw-cap glass vials or flame-sealed glass ampoules. The $HClO_4$ solutions were chosen to probe the effects of pH on the reactivity and distribution of water radiolysis products, since ClO_4^- is essentially radiolytically inert.[43]

Multiscale computational modelling

A combination of Monte Carlo radiation track[35,36] and independent reaction times (IRT)[37] models, in conjunction with a deterministic kinetic model, were used to construct a multiscale predictive computer model for the radical-induced oxidative and reductive behavior of AHA in aqueous solutions.[44,45] Calculated stochastic radiation track yields, listed in ESI Table S1† were used as inputs for the deterministic kinetic model, which represents chemical mechanistic reactions as coupled differential equations that are solved numerically using the FACSIMILE kinetic modelling software package.[46] The chemical kinetic reaction set used by these calculations consisted of an existing reaction scheme for water radiolysis[28] supplemented by radical reactions for AHA and its degradation products, as summarized in ESI Table S2.† Where available, Arrhenius parameters were incorporated to accommodate for changes in temperature between irradiations. Gas partitioning between the aqueous and gaseous phases was accounted for using a simple stagnant two-film model[47] with standard Henry's law coefficients[48] and temperature-dependent diffusion parameters.[49–52]

Results and discussion

Radical reaction kinetics

The radiolytic degradation of AHA is driven by a combination of radical-induced oxidation and reduction processes in the aqueous solutions investigated by this work. The second-order rate coefficients (k) of these radical-induced reactions with the protonated and deprotonated forms of AHA ($pK_a = 8.7$ at 25 °C) and its major degradation product HA, were determined, or re-evaluated, at different pHs to quantify their relative contributions. The radical-induced chemical reactions of acetic acid, the other major AHA hydrolysis product (eqn (1)), have been well-studied and their rates are considered established, therefore they did not require measurement for inclusion in the model developed in this work.[53–61] Although there are a few possible isomers of AHA, only the Z-amide is considered in this work as it is the most stable form in aqueous solution.[62,63]

Typical data from the electron pulse kinetic measurements from this study are presented in Fig. 1 for the reaction of HA with the e_{aq}^-. All other kinetic data are given in ESI Fig. S4–S8.† The second-order rate coefficients derived from these measurements are listed in Table 1. These rate values were incorporated into the multiscale modelling chemical kinetic reaction set, as outlined in the ESI.†

Radical-induced degradation mechanism of acetohydroxamic acid

The loss of 0.50 M AHA under gamma irradiation in aerated water and 0.20 M $HClO_4$ aqueous solution is shown in Fig. 2.
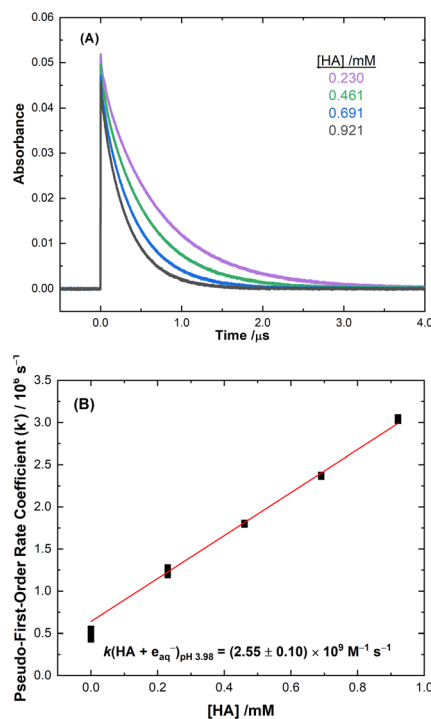

Fig. 1 (A) Measured kinetic decay traces of the e_{aq}^- at 720 nm for electron pulse irradiated solutions at room temperature for: 0.230 (purple), 0.461 (green), 0.691 (blue), and 0.921 (black) mM HA. (B) Second-order rate coefficient determination from the pseudo-first-order values obtained for each HA concentration for the reaction of HA with the e_{aq}^-. The weighted linear fit corresponds to a second-order reaction rate coefficient of k (HA + e_{aq}^-) = (2.55 ± 0.10) × 10^9 M^{-1} s^{-1}, R^2 = 0.996.
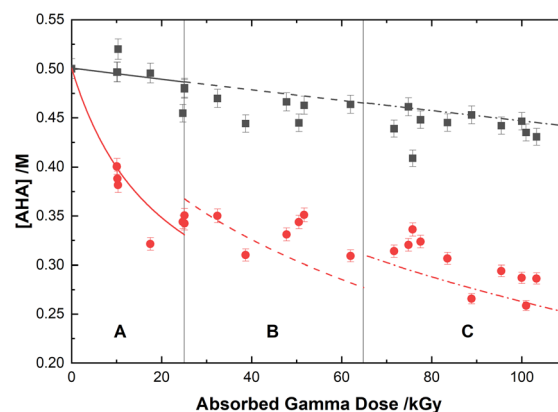

Fig. 2 Concentration of 0.50 M AHA as a function of absorbed gamma dose in water (■), and 0.20 M $HClO_4$ (●). The experimental data points are divided into three regions: (A) 51 Gy min^{-1} at 36 °C (solid curve); (B) 150 Gy min^{-1} at 40 °C (dashed curve); and (C) 250 Gy min^{-1} at 42 °C (dash–dot curve). Lines are predicted values from multiscale modelling calculations.
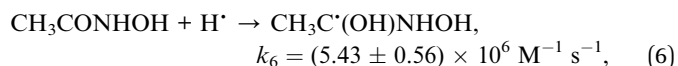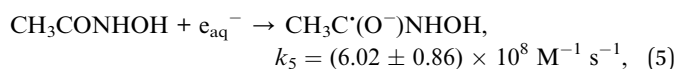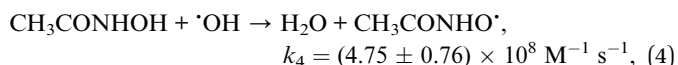
Multiscale computer model predictions are plotted alongside the experimental data and are in excellent agreement for both solutions. Model predictions are broken into three distinct

Table 1 Measured second-order rate coefficients (k) for the reactions of the protonated (CH$_3$CONHOH) and deprotonated (CH$_3$CONHO$^-$) forms of AHA (pK_a = 8.7) and NH$_3$OH$^+$ (pK_a = 6.17) with the e$_{aq}^-$, H$^\bullet$ atom, and $^\bullet$OH radical at room temperature

| Radical species	Second-order rate coefficient (k, M^{-1} s^{-1})		
	CH$_3$CONHOH	CH$_3$CONHO$^-$	NH$_3$OH$^+$
e$_{aq}^-$	$(6.02 \pm 0.86) \times 10^8$ —		$(2.55 \pm 0.10) \times 10^9$
H$^\bullet$	$(5.43 \pm 0.56) \times 10^6$ —		$(4.01 \pm 0.43) \times 10^5$
$^\bullet$OH	$(4.75 \pm 0.76) \times 10^8$	$(3.86 \pm 0.11) \times 10^9$	$(1.59 \pm 0.06) \times 10^9$

'regions' chosen as representatives for the specific experimental conditions under which these measurements were performed: Region A, from 0–25 kGy is for a constant temperature of T = 36 °C at 51 Gy min^{-1}; Region B from 25–65 kGy is for a constant temperature of T = 40 °C at 150 Gy min^{-1}; and Region C from 65–110 kGy is for a constant temperature of T = 42 °C at 250 Gy min^{-1}. These three sets of experimental conditions were chosen to keep the hydrolysis time relatively consistent between irradiations. The different regions are separated by vertical lines in Fig. 2, and the change in model conditions are indicated by changes in the line style (solid, dash, and dash–dot) used in the plot. AHA is consumed as a function of absorbed gamma dose and time in both aqueous solutions because of a combination of radiolysis and hydrolysis. This behavior is linear as a function of dose for H$_2$O, but the loss is much more rapid in the HClO$_4$ solution due to the hydrolysis reaction (eqn (1)).

The mechanisms for the radical-induced degradation of AHA can be better understood from viewing the cumulative reaction outputs, *i.e.*, the sum concentration of products produced by a given reaction, as shown in Fig. 3. For AHA in aerated water, Fig. 3(A), the radiolytic loss of AHA proceeds primarily *via* its reaction with the major radical products from water radiolysis (*i.e.*, AHA is lost by reaction with the $^\bullet$OH radical (48.7%), e$_{aq}^-$ (46.5%), and H$^\bullet$ atom (4.6%), at 100 kGy) according to the reactions:

$$CH_3CONHOH + {}^\bullet OH \rightarrow H_2O + CH_3CONHO^\bullet,$$
$$k_4 = (4.75 \pm 0.76) \times 10^8 \text{ M}^{-1} \text{ s}^{-1}, \quad (4)$$

$$CH_3CONHOH + e_{aq}^- \rightarrow CH_3C^\bullet(O^-)NHOH,$$
$$k_5 = (6.02 \pm 0.86) \times 10^8 \text{ M}^{-1} \text{ s}^{-1}, \quad (5)$$

$$CH_3CONHOH + H^\bullet \rightarrow CH_3C^\bullet(OH)NHOH,$$
$$k_6 = (5.43 \pm 0.56) \times 10^6 \text{ M}^{-1} \text{ s}^{-1}, \quad (6)$$

where the product of eqn (6) is discussed below in the context of the gaseous products. The carbon-centered radical anion produced in eqn (5) is expected to protonate to CH$_3$C$^\bullet$(OH) NHOH. Under oxygenated conditions, it would then react quickly with dissolved oxygen to produce a peroxyl radical, which would then undergo a second-order combination with itself to form a tetroxide intermediate.[64–66] The tetroxide species would break apart to form O$_2$ and two alkoxyl radicals,[66] which would ultimately hydrolyze to form CH$_3$COOH and NH$_2$O$^\bullet$.[67]

The oxygen in our system is quickly depleted, and in the absence of oxygen, the protonated alkoxy radical product will primarily undergo β-scission[68] as follows:

$$CH_3C^\bullet(OH)NHOH \rightarrow CH_3CHO + NH_2O^\bullet,$$
$$k_7 = 1 \times 10^7 \text{ M}^{-1} \text{ s}^{-1}. \quad (7)$$
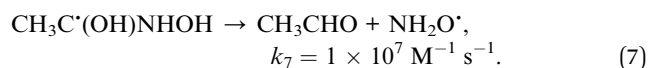
The rate coefficient for k_7 is approximated by the rates of similar reactions.[67,69,70] The acetaldehyde (CH$_3$CHO) that is formed is expected to react with the primary radiolysis products of water,[55,71,72] primarily by oxidizing to acetic acid, and to speciate *via* its own equilibria[73] and acidic degradation reactions[74] in solution.

AHA is also expected to react with other minor radical products generated in the solution such as $^\bullet$CH$_2$COOH, $^\bullet$CH$_3$, and $^\bullet$CONHOH. The transient nitroxide radical (CH$_3$CONHO$^\bullet$), formed in the AHA reaction with the $^\bullet$OH radical and other minor carbon radical species undergoes bimolecular combination according to eqn (3), resulting in an acyl nitroso (CH$_3$CON=O). Acyl nitroso compounds are unstable and have been shown to undergo hydrolysis as follows:[75,76]

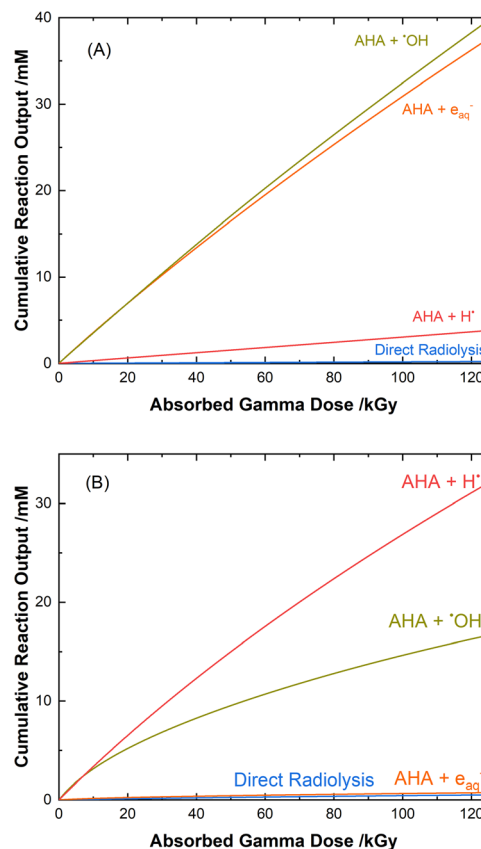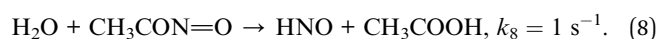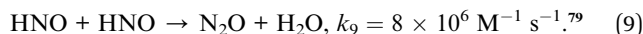$$H_2O + CH_3CON{=}O \rightarrow HNO + CH_3COOH, \quad k_8 = 1 \text{ s}^{-1}. \quad (8)$$

Fig. 3 Multiscale model calculated cumulative reaction outputs for the major pathways involved in the radical-induced loss of 0.5 M AHA for 51 Gy min^{-1} at 36 °C in (A) water and (B) 0.20 M HClO$_4$.

The HNO formed undergoes bimolecular combination with itself to ultimately yield H_2O and N_2O according to:[77–79]

$$HNO + HNO \rightarrow N_2O + H_2O, \quad k_9 = 8 \times 10^6 \text{ M}^{-1} \text{ s}^{-1}.[79] \quad (9)$$

Finally, there is also a small contribution from the direct radiolysis of AHA, *i.e.*, the direct deposition of ionizing radiation energy into the electrons of AHA. Calculations based on the electron density of AHA predict that less than 4% of the gamma radiation would interact directly with AHA molecules.[29] From these interactions, the AHA can become excited or ionized, resulting in different breakdown pathways to form a variety of products. One pathway suggested in the literature is:[31]

$$CH_3CONHOH \rightsquigarrow CH_3CONHOH^* \rightarrow {}^{\bullet}CONHOH + {}^{\bullet}CH_3, \quad (10)$$
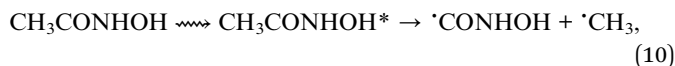
the products of which ultimately result in the formation of HA, HCOOH, and CH_4, all of which were detected in the characterization methods used by this work. The *G*-value for this pathway was found to be 0.05 μmol J^{-1} in H_2O, and 0.21 μmol J^{-1} in $HClO_4$ by optimizing to fit the HCOOH and CH_4 detected experimentally, as shown in ESI Fig. S9.†

Fig. 3(B) shows the cumulative reaction yields for the radiation-induced degradation of AHA in 0.20 M $HClO_4$. Since the perchlorate anion is essentially radiolytically inert under the given conditions,[43] the reaction set here is much the same as for water, and proceeds *via* the same primary radical species. One major difference, however, is the low solution pH (∼0.7). At low pH, the excess of protons (H_{aq}^+) alters the suite of water radiolysis products (ESI Table S1†), predominantly converting the yield of the e_{aq}^- into $H^{\bullet}$ atom *via* the fast reaction:

$$e_{aq}^- + H_{aq}^+ \rightarrow H^{\bullet}, \quad k_{11} = 2.3 \times 10^{10} \text{ M}^{-1} \text{ s}^{-1}.[27] \quad (11)$$
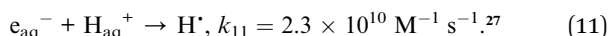
Although both the e_{aq}^- and $H^{\bullet}$ atom can be powerful reductants, the $H^{\bullet}$ atom can undergo addition and abstraction reactions with organic molecules, resulting in different product distributions.[27] Further, under these acidic conditions the majority of AHA loss in solution is due to hydrolysis (eqn (1)) as opposed to radical-induced processes. As shown in Fig. 4, the predicted relative contributions of hydrolysis and radiolysis as a function of absorbed dose for 0.50 M AHA in 0.20 M $HClO_4$ irradiated at a rate of 51 Gy min^{-1} at 36 °C amounts to 85% and 15%, respectively at 100 kGy.

Overview of aqueous degradation products

Based on the above reaction schemes, the major aqueous products of AHA degradation under the given conditions are acetic acid and HA, formed from both the radiolysis and hydrolysis processes. Although the yields of these two species from hydrolysis are equimolar, HA is negligibly produced from the radiolysis reactions. Further, both hydrolysis products react at different rates with the various aforementioned radicals, resulting in differences in their overall steady-state yields and subsequent degradation product distributions. The in-growth of acetic acid and HA from the degradation of 0.50 M AHA in
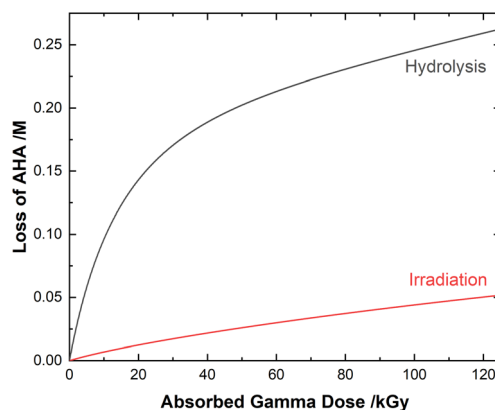

Fig. 4 Multiscale model calculated relative contributions of hydrolysis and gamma radiolysis reactions to the cumulative loss of 0.50 M AHA for 51 Gy min^{-1} at 36 °C in 0.20 M $HClO_4$.

water and 0.20 M $HClO_4$ are shown in Fig. 5 and 6, respectively. Our multiscale model predictions are plotted alongside experimental data and again are in excellent agreement. In both solutions there is more acetic acid formed than HA, consistent with the stoichiometry predicted by Sanchez-Garcia *et al.*[80] As expected, more acetic acid and HA are formed in the $HClO_4$ solution than in water due to the increased rate of AHA hydrolysis. There was no NO_2^- or HNO_2 detected in these systems by IC or UV-vis methods.

Radical-induced degradation mechanism of hydroxylamine

The cumulative reaction yields for the loss of HA as a function of absorbed gamma dose for each of the two solution conditions are shown in Fig. 7. The primary contributors to the degradation of HA in water, as shown in Fig. 7(A), are its reaction with
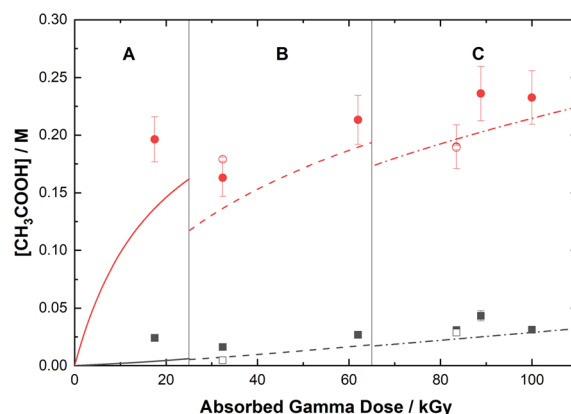

Fig. 5 Yields of acetic acid from the gamma irradiation of 0.50 M AHA in water (■) and 0.20 M $HClO_4$ (●). The experimental data are from IC (filled symbols) and ^{1}H-NMR (open symbols) and are divided into three regions: (A) 51 Gy min^{-1} at 36 °C (solid curve), (B) 150 Gy min^{-1} at 40 °C (dashed curve), and (C) 250 Gy min^{-1} at 42 °C (dash–dot curve). Lines are predicted values from multiscale modelling calculations.
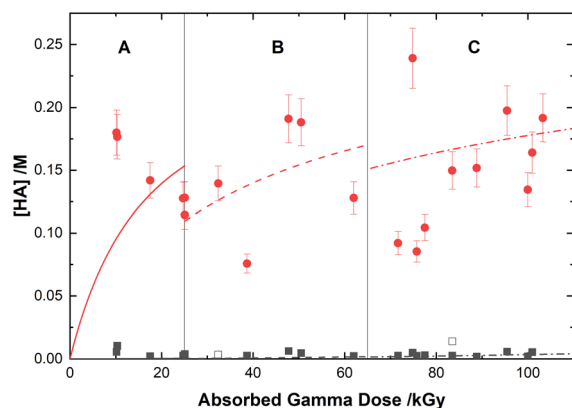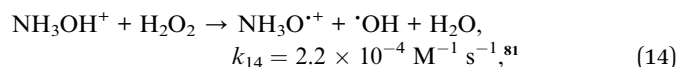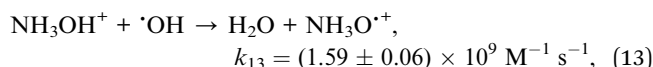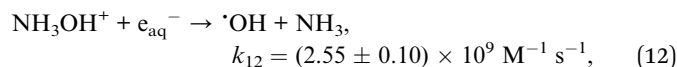
Fig. 6 Yields of HA from the gamma irradiation of 0.50 M AHA in water (■) and 0.20 M $HClO_4$ (●). The experimental data are from UV-vis spectroscopy (filled symbols) and ^{1}H-NMR (open symbols), and are divided into three regions: (A) 51 Gy min^{-1} at 36 °C (solid curve), (B) 150 Gy min^{-1} at 40 °C (dashed curve), and (C) 250 Gy min^{-1} at 42 °C (dotted curve). Lines are predicted values from multiscale modelling calculations.

the e_{aq}^- (53% at 100 kGy), the $^•OH$ radical (45% at 100 kGy), and its molecular reaction with H_2O_2 (2% at 100 kGy):

$$NH_3OH^+ + e_{aq}^- \rightarrow {}^•OH + NH_3,$$
$$k_{12} = (2.55 \pm 0.10) \times 10^9 \text{ M}^{-1} \text{ s}^{-1}, \quad (12)$$

$$NH_3OH^+ + {}^•OH \rightarrow H_2O + NH_3O^{•+},$$
$$k_{13} = (1.59 \pm 0.06) \times 10^9 \text{ M}^{-1} \text{ s}^{-1}, \quad (13)$$

$$NH_3OH^+ + H_2O_2 \rightarrow NH_3O^{•+} + {}^•OH + H_2O,$$
$$k_{14} = 2.2 \times 10^{-4} \text{ M}^{-1} \text{ s}^{-1}, [81] \quad (14)$$

where this oxidant predominately arises from the recombination of the $^•OH$ radical in the radiation track, with its escape yield as given in ESI Table S1†.[81] The k_{14} rate coefficient was determined by Chen *et al.*[81] and found to be consistent with benchtop reactions of H_2O_2 and HA as shown in ESI Fig. S10.† It should be noted that the reaction given in eqn (12), although originally proposed[82] to produce $^•NH_3^+$ and OH^-, has since been demonstrated by Neta *et al.*[83] to occur as given here.

For 0.20 M $HClO_4$, as shown in Fig. 7(B), a significant portion of the e_{aq}^- yield is converted to $H^•$ atom (eqn (11)). This allows for its reaction with HA to have an additional contribution to the overall loss of HA:

$$NH_3OH^+ + H^• \rightarrow H_2 + NH_3O^{•+},$$
$$k_{15} = (4.01 \pm 0.43) \times 10^5 \text{ M}^{-1} \text{ s}^{-1}. \quad (15)$$
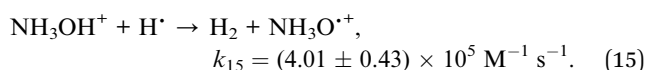
The HA radical formed in these reactions was originally proposed to take the form $^•NHOH/^•NH_2OH^+$.[82,84,85] However, it has since been shown by EPR studies and quantum chemical calculations that the more thermodynamically stable isomer is $NH_2O^•/NH_3O^{•+}$.[81,86,87] Decay of $NH_2O^•$ proceeds by one of several competing pathways, yielding either N_2 or N_2O as gaseous products. Under anoxic conditions, we have:[88]
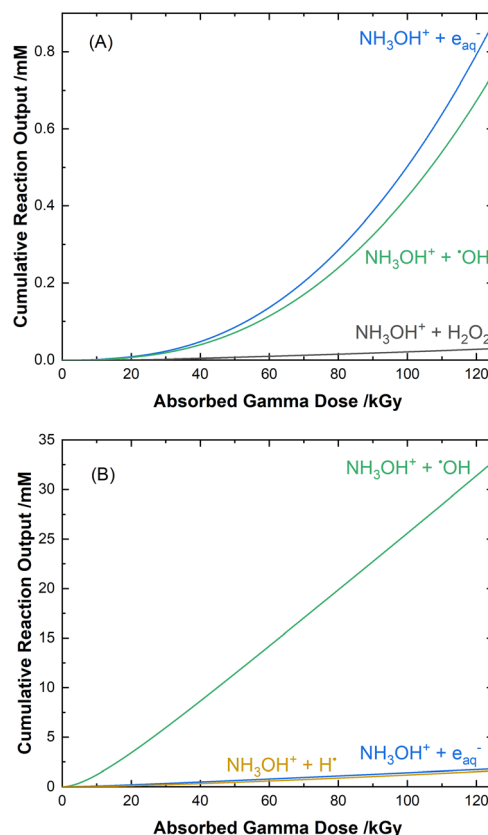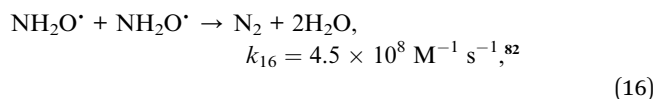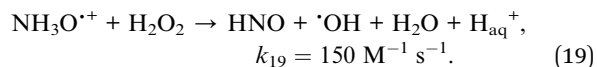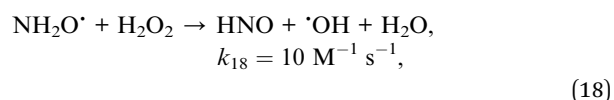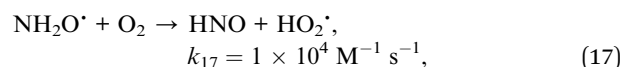

Fig. 7 Calculated cumulative reaction yields for the major pathways involved in the radiolytic loss of HA for 51 Gy min^{-1} gamma irradiation at 36 °C in 0.5 M AHA in (A) water, and (B) 0.20 M $HClO_4$.

$$NH_2O^• + NH_2O^• \rightarrow N_2 + 2H_2O,$$
$$k_{16} = 4.5 \times 10^8 \text{ M}^{-1} \text{ s}^{-1}, [82] \quad (16)$$

and under aerated conditions, the following reactions must also be considered:[88]

$$NH_2O^• + O_2 \rightarrow HNO + HO_2^•,$$
$$k_{17} = 1 \times 10^4 \text{ M}^{-1} \text{ s}^{-1}, \quad (17)$$

$$NH_2O^• + H_2O_2 \rightarrow HNO + {}^•OH + H_2O,$$
$$k_{18} = 10 \text{ M}^{-1} \text{ s}^{-1}, \quad (18)$$

$$NH_3O^{•+} + H_2O_2 \rightarrow HNO + {}^•OH + H_2O + H_{aq}^+,$$
$$k_{19} = 150 \text{ M}^{-1} \text{ s}^{-1}. \quad (19)$$

Although reactions eqn (17)–(19) have been proposed in the literature,[81,82,84,88] their rates have not been reported. In our model, the rates of these reactions were optimized to match the experimental production of N_2O. In agreement with these optimized values, Simic and Hayon suggest that the rate coefficient for reaction eqn (18) is likely slower than eqn (19),[82] and Karpel Vel Leitner *et al.*[88] found that eqn (19) did not occur significantly under their experimental conditions.

Table 2 G-values for the gaseous products resulting from the irradiation of 0.50 M AHA in water and in 0.20 M HClO$_4$

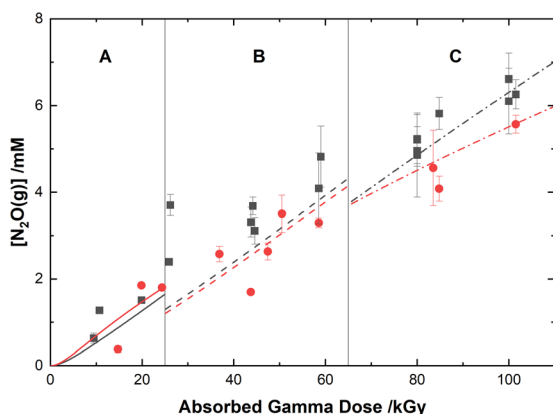|	Experimental gas yields (G-values) in µmol J^{-1}	
	Water	0.20 M HClO$_4$
N$_2$O	0.076 ± 0.003	0.061 ± 0.005
H$_2$	0.045 ± 0.002	0.139 ± 0.015
CH$_4$	0.0016 ± 0.0002	0.0075 ± 0.0005

The HNO produced in eqn (17)–(19) undergoes bimolecular combination according to eqn (9) and therefore, in both solutions, the HA that reacts is primarily converted into N$_2$O and H$_2$O.

### Overview of gaseous degradation products

The measured G-values (yields) for the gaseous species resulting from the irradiation of aqueous solutions of AHA are listed in Table 2. The yield of CH$_4$ is very low, as it is produced only from the direct radiolysis of AHA (eqn (10)), which, based on electron fraction calculations, should receive less than 4% of the total gamma radiation at a concentration of 0.50 M. The relative order of magnitude of the G-values for the three gaseous products agree with the volume fraction ratios suggested by Wang *et al.*[31]

The experimental yields of the major gaseous products, N$_2$O and H$_2$, are shown with our computer model predictions in Fig. 8 and 9, respectively. As shown in Fig. 8, the calculations agree well with the measured yields of N$_2$O and demonstrate a small reduction in this yield for the HClO$_4$ solutions as compared to pure water.

Our cal culations show that H$_2$ is primarily produced from water radiolysis. These radiolytic yields have been extensively investigated in aqueous systems and are attributed to a series of reactions involving H$_2$O, the e$_{aq}^-$, and the H$^{\bullet}$ atom.[89] Our model
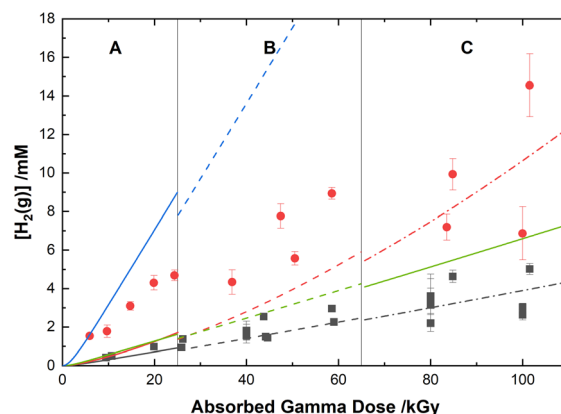
Fig. 9 Yields of H$_2$ from the gamma irradiation of 0.50 M AHA in water (■) and 0.20 M HClO$_4$ (●). The experimental data are divided into three regions: (A) 51 Gy min^{-1} at 36 °C (solid curve), (B) 150 Gy min^{-1} at 40 °C (dashed curve), and (C) 250 Gy min^{-1} at 42 °C (dash–dot curve). Lines are predicted values from multiscale modelling calculations using eqn (20) (blue, green) and eqn (21) (red, black) for the reaction of AHA + H$^{\bullet}$ in 0.20 M HClO$_4$ and H$_2$O respectively.

predicts higher H$_2$ yields at lower pH, as expected due to an increase in H$^{\bullet}$ atom yield under these conditions (as per eqn (11)). In the presence of AHA, there are additional contributions to the yield of H$_2$ from H-atom abstraction reactions with the hydrolysis products acetic acid and HA, and with the radiolytic product acetaldehyde. Wang *et al.*[31] proposed an analogous H-abstraction reaction for AHA:

$$CH_3CONHOH + H^{\bullet} \rightarrow H_2 + CH_3CONHO^{\bullet}, \quad (20)$$
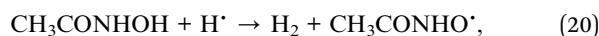
However, our model predicts that if the products of this reaction included H$_2$, the G-value for H$_2$ in water would be ~1.5× the experimentally determined value of 0.045 µmol J^{-1}. This result is demonstrated by the blue and green curves in Fig. 9 for 0.20 M HClO$_4$ and H$_2$O respectively. Therefore, considering the level of agreement between multiscale model calculations and experiment demonstrated thus far, the pathway proposed by Wang *et al.*[31] is not considered to be the major mechanism. Furthermore, in an experiment measuring CH$_3$CONHO$^{\bullet}$ Samuni and Goldstein[32] were unable to assign products to the reaction between H$^{\bullet}$ and AHA, and therefore the nitroxide radical is also unlikely to be significantly produced. Accordingly, the reaction of AHA and H$^{\bullet}$ is proposed to proceed primarily *via*:

$$CH_3CONHOH + H^{\bullet} \rightarrow CH_3C^{\bullet}(OH)NHOH, \quad (21)$$

which yields more accurate H$_2$ yields for 0.50 M AHA in water and 0.20 M HClO$_4$. The radical formed in this reaction is the same as the protonated form of the radical from the reaction of AHA and the e$_{aq}^-$, and it will react primarily according to eqn (7) under the given conditions.

All these reactions together provide a detailed picture of the degradation of AHA in acidic aqueous solutions *via* free radical

Fig. 8 Yields of N$_2$O from the gamma irradiation of 0.50 M AHA in water (■) and 0.20 M HClO$_4$ (●). The experimental data are divided into three regions: (A) 51 Gy min^{-1} at 36 °C (solid curve), (B) 150 Gy min^{-1} at 40 °C (dashed curve), and (C) 250 Gy min^{-1} at 42 °C (dash–dot curve). Lines are predicted values from multiscale modelling calculations.

reactions. The foundational aqueous solution model developed in this work can be further developed to apply to specific applications, as this model has been shown to agree with changes in pH and rate of radical generation at moderate temperatures above ambient conditions. For example, this model could be adapted for use under physiological conditions where the primary radicals generated are reactive oxygen and nitrogen species, because radicals like O_2^- and $^\bullet NO_2$ do not react with AHA, and $RO^\bullet$ species like $^\bullet CO_3^-$ will yield the same AHA oxidation product as $^\bullet OH$.[32]

Conclusions

A multiscale computer model has been developed and rigorously evaluated against experimental results for the prediction of the radical-induced behavior of AHA in aqueous solutions. Both calculations and experiment demonstrate that: (i) the major products of AHA degradation in acidic aqueous solution are acetic acid, HA, N_2O, and H_2, with formic acid and CH_4 as additional minor products; (ii) hydrolysis plays a more significant role in the decomposition of AHA than radiolysis under highly acidic conditions; (iii) the radical-induced AHA degradation occurs predominantly through oxidation by the $^\bullet OH$ radical and reduction by the e_{aq}^-, with an increasing contribution from the $H^\bullet$ atom with decreasing pH. The computational model developed in this work can be used to accurately predict the degradation behavior of AHA in simple acidic aqueous solutions.

Beyond the current work, this modelling methodology has been shown to be extremely effective in providing quantitative mechanistic insight into the radiation chemistry occurring over multiple time and distance regimes—from the point of energy deposition, through the lifetime of the non-homogenous radiation chemical track, and ultimately bulk solution—for several aqueous systems including nitrate and nitric acid in the absence[44] and presence of neptunium[90] and americium[91] ions, and for organic molecules, including diglycolamides.[92] The proof of principle of these multiscale models has again been demonstrated by the agreement here between calculation and experiment over changes in pH, temperature, and dose rate. This ultimately demonstrates the power of this type of modelling methodology, which will be expanded in future works to apply to different types of chemistry occurring in aqueous solutions and beyond.

Author contributions

Jacy K. Conrad played the lead role in developing experimental methodology for the analytical techniques, steady state gamma irradiation data collection and analysis, kinetic model development and validation, and writing the original draft. Corey D. Pilgrim conducted the NMR data collection and analysis. Simon M. Pimblott developed the stochastic model and calculated the radiolytic escape yields. Simon M. Pimblott and Gregory P. Horne developed the multiscale model foundation. Gregory P. Horne and Stephen P. Mezyk collected the electron pulse radiolysis kinetic data and added valuable insights in the reaction mechanisms and the writing review and editing.

Gregory P. Horne played a supervisory role in the kinetic model development and validation and lead the funding acquisition and conceptualization.

Conflicts of interest

There are no conflicts to declare.

Acknowledgements

References

1 S. Goldstein and A. Samuni, in *Advances in Inorganic Chemistry*, ed. R. van Eldik and J. A. Olabe, Academic Press, 2015, vol. 67, ch. 8, pp. 315–333.

2 Z. Syed, K. Sonu, A. Dongre, G. Sharma and M. Sogani, *Int. J. Biol. Biomed.*, 2020, **14**, 75–88.

3 B. R. Kant, B. S. Kant, B. T. Chand and B. A. Kumar, in *Microbial Applications*, ed. V. Kalia, Springer, Cham, 2017, vol. 2.

4 J. Keth, T. Johann and H. Frey, *Biomacromolecules*, 2020, **21**, 2546–2556.

5 R. J. Taylor, I. May, A. L. Wallwork, I. S. Denniss, N. J. Hill, B. Y. Galkin, B. Y. Zilberman and Y. S. Fedorov, *J. Alloys Compd.*, 1998, **271**, 534–537.

6 I. May, R. J. Taylor and G. Brown, *J. Alloys Compd.*, 1998, **271**, 650–653.

7 I. May, R. J. Taylor, I. S. Denniss, G. Brown, A. L. Wallwork, N. J. Hill, J. M. Rawson and R. Less, *J. Alloys Compd.*, 1998, **275**, 769–772.

8 P. Tkac, B. Matteson, J. Bruso and A. Paulenova, *J. Radioanal. Nucl. Chem.*, 2008, **277**, 31–36.

9 C. Marwick, *JAMA*, 1983, **250**, 321–322.

10 W. N. Fishbein and P. P. Carbone, *J. Biol. Chem.*, 1965, **240**, 2407–2414.

11 J. L. Domingo, *Reprod. Toxicol.*, 1998, **12**, 499–510.

12 M. E. Neganova, S. G. Klochkov, Y. R. Aleksandrova and G. Aliev, *Curr. Med. Chem.*, 2021, **28**, 8139–8162.

13 C. Adamson, H. Kajino, S. A. Kawashima, K. Yamatsugu and M. Kanai, *J. Am. Chem. Soc.*, 2021, **143**, 14976–14980.

14 V. N. Osipov, D. S. Khachatryan and A. N. Balaev, *Med. Chem. Res.*, 2020, **29**, 831–845.

15 D. V. Stanisheva, G. Atanasov, M. D. Aposstolova and O. I. Petrov, *Curr. Bioact. Compd.*, 2021, **17**, 59–66.

16 A. Citarella, D. Moi, L. Pinzi, D. Bonanni and G. Rastelli, *ACS Omega*, 2021, **6**, 21843–21849.

17 F. P. L. Andrieux, C. Boxall and R. J. Taylor, *J. Solution Chem.*, 2008, **37**, 1511–1527.

18 F. P. L. Andrieux, C. Boxall, H. M. Steele and R. J. Taylor, *J. Solution Chem.*, 2014, **43**, 608–622.

19 I. Sanchez-Garcia, L. J. Bonales, H. Galan, J. M. Perlado and J. Cobos, *Spectrochim. Acta, Part A*, 2020, **229**, 117877–117883.

20 Y. Arun, M. Daifa and A. J. Domb, *Polym. Adv. Technol.*, 2021, **32**, 842–852.

21 Y. J. Chen, J. S. Ye, Y. Chen, H. Hu, H. L. Zhang and H. S. Ou, *Chem. Eng. J.*, 2019, **356**, 98–106.

22 G. Moussavi, E. Fathi and M. Moradi, *Process Saf. Environ. Prot.*, 2019, **126**, 259–268.

23 W. J. Cooper, S. P. Mezyk, J. R. Peller, S. K. Cole, W. H. Song, B. J. Mincher and B. M. Peake, *Ozone: Sci. Eng.*, 2008, **30**, 58–64.

24 P. Gehringer and H. Eschweiler, in *Environmental Applications of Ionizing Radiation*, ed. W. J. Cooper, R. D. Curry and K. E. O'Shea, Wiley Interscience, New York, 1998, ch. 20, pp. 325–341.

25 T. Oppenländer, *Photochemical Purification of Water and Air: Advanced Oxidation Processes (AOPs) – Principles, Reaction Mechanisms, Reactor Concepts*, Wiley-VCH Verlag, Weinheim, Germany, 2007.

26 H. Zhou and D. W. Smith, *J. Environ. Eng. Sci.*, 2002, **1**, 247–264.

27 G. V. Buxton, C. L. Greenstock, W. P. Helman and A. B. Ross, *J. Phys. Chem. Ref. Data*, 1988, **17**, 513–886.

28 A. J. Elliot and D. M. Bartels, *The Reaction Set, Rate Constants and G-Values for the Simulation of the Radiolysis of Light Water Over the Range 20° to 350 °C Based on Information Available in 2008*, Report 153-127160-450-001, AECL Nuclear Platform Research and Development, 2009.

29 J. W. T. Spinks and R. J. Woods, *Introduction to Radiation Chemistry*, John Wiley & Sons Inc., Canada, 3rd edn, 1990.

30 D. G. Karraker, *Radiation Chemistry of Acetohydroxamic Acid in the UREX Process*, United States, 2002.

31 J. H. Wang, C. Li, Q. Li, M. H. Wu, W. F. Zheng and H. He, *Nucl. Sci. Technol.*, 2018, **29**, 27–35.

32 A. Samuni and S. Goldstein, *J. Phys. Chem. A*, 2011, **115**, 3022–3028.

33 M. Gabricevic, E. Besic, M. Birus, A. Zahl and R. van Eldik, *J. Inorg. Biochem.*, 2006, **100**, 1606–1613.

34 W. Chamulitrat, R. P. Mason and D. Riendeau, *J. Biol. Chem.*, 1992, **267**, 9574–9579.

35 S. M. Pimblott, J. A. LaVerne and A. Mozumder, *J. Phys. Chem.*, 1996, **100**, 8595–8606.

36 S. M. Pimblott and J. A. LaVerne, *J. Phys. Chem. A*, 2002, **106**, 9420–9427.

37 P. Clifford, N. J. B. Green, M. J. Oldfield, M. J. Pilling and S. M. Pimblott, *J. Chem. Soc., Faraday Trans. 1*, 1986, **82**, 2673–2689.

38 J. F. Wishart, A. R. Cook and J. R. Miller, *Rev. Sci. Instrum.*, 2004, **75**, 4359–4366.

39 G. L. Hug, Y. C. Wang, C. Schoneich, P. Y. Jiang and R. W. Fessenden, *Radiat. Phys. Chem.*, 1999, **54**, 559–566.

40 K. Whitman, S. Lyons, R. Miller, D. Nett, P. Treas, A. Zante, R. W. Fessenden, M. D. Thomas and Y. Wang, Linear accelerator for radiation chemistry research at Notre Dame, *Proceedings of the '95 Particle Accelerator Conference and International Conference on High Energy Accelerators*, Dallas, Texas, USA, 1996.

41 G. V. Buxton and C. R. Stuart, *J. Chem. Soc., Faraday Trans.*, 1995, **91**, 279–281.

42 H. Fricke, E. J. Hart and H. P. Smith, *J. Chem. Phys.*, 1938, **6**, 229–240.

43 M. Domae, Y. Katsumura, P. Y. Jiang, R. Nagaishi, K. Ishigure, T. Kozawa and Y. Yoshida, *J. Chem. Soc., Faraday Trans.*, 1996, **92**, 2245–2250.

44 G. P. Horne, T. A. Donoclift, H. E. Sims, R. M. Orr and S. M. Pimblott, *J. Phys. Chem. B*, 2016, **120**, 11781–11789.

45 G. Garaix, G. P. Horne, L. Venault, P. Moisy, S. M. Pimblott, J. L. Marignier and M. Mostafavi, *J. Phys. Chem. B*, 2016, **120**, 5008–5014.

46 *MCPA Software FACSIMILE Kinetic Modeling Software Package*.

47 W. G. Whitman, *Chem. Metall. Eng.*, 1923, **26**, 146–148.

48 R. Sander, Henry's Law Constants, in *NIST Chemistry WebBook*, NIST Standard Reference Database Number 69, ed. P. J. Linstrom and W. G. Mallard, National Institute of Standards and Technology, Gaithersburg MD, 2018.

49 D. T. Kallikragas, A. Y. Plugatyr and I. M. Svishchev, *J. Chem. Eng. Data*, 2014, **59**, 1964–1969.

50 A. Tamimi, E. B. Rinker and O. C. Sandall, *J. Chem. Eng. Data*, 1994, **39**, 330–332.

51 W. J. Massman, *Atmos. Environ.*, 1998, **32**, 1111–1127.

52 H. Moradi, H. Azizpour, H. Bahmanyar, M. Mohammadi and M. Akbari, *Heliyon*, 2020, **6**, 5385.

53 D. Razem and W. H. Hamill, *J. Phys. Chem.*, 1977, **81**, 1625–1631.

54 J. K. Thomas, *Trans. Faraday Soc.*, 1965, **61**, 702–707.

55 P. Neta, R. W. Fessenden and R. H. Schuler, *J. Phys. Chem.*, 1971, **75**, 1654–1666.

56 M. Exner, H. Herrmann and R. Zellner, *J. Atmos. Chem.*, 1994, **18**, 359–378.

57 M. J. Davies, B. C. Gilbert, C. B. Thomas and J. Young, *J. Chem. Soc., Perkin Trans.*, 1985, **2**, 1199–1204.

58 G. Kohler, S. Solar, N. Getoff, A. R. Holzwarth and K. Schaffner, *J. Photochem.*, 1985, **28**, 383–391.

59 P. Neta and R. H. Schuler, *J. Phys. Chem.*, 1972, **76**, 2673–2679.

60 R. L. Willson, C. L. Greenstock, G. E. Adams, R. Wageman and L. M. Dorfman, *Int. J. Radiat. Phys. Chem.*, 1971, **3**, 211–220.

61 P. Neta and R. H. Schuler, *J. Phys. Chem.*, 1975, **79**, 1–6.

62 M. L. Senent, A. Nino, C. M. Caro, S. Ibeas, B. Garcia, J. M. Leal, F. Secco and M. Venturini, *J. Org. Chem.*, 2003, **68**, 6535–6542.

63 S. Tolosa, N. Mora-Diez, A. Hidalgo and J. A. Sanson, *RSC Adv.*, 2014, **4**, 44757–44768.

64 J. A. Howard and J. E. Bennett, *Can. J. Chem.*, 1972, **50**, 2374–2377.

65 G. A. Russell, *J. Am. Chem. Soc.*, 1957, **79**, 3871–3877.

66 L. M. Smith, H. M. Aitken and M. L. Coote, *Acc. Chem. Res.*, 2018, **51**, 2006–2013.

67 P. Neta and A. B. Ross, *J. Phys. Chem. Ref. Data*, 1990, **19**, 413–512.

68 E. Suáres and M. Rodriguez, in *Radicals in Organic Synthesis*, ed. P. Renaud and M. P. Sibi, Wiley-VCH, Weinheim, 2001, vol. 2, p. 440.

69 M. Murakami and N. Ishida, *Chem. Lett.*, 2017, **46**, 1692–1700.

70 M. Bietti, O. Lanzalunga and M. Salamone, *J. Org. Chem.*, 2005, **70**, 1417–1422.

71 C. S. Satterfield and L. C. Case, *Ind. Eng. Chem.*, 1954, 998–1001.

72 G. Duplatre and C. D. Jonah, *Radiat. Phys. Chem.*, 1984, **24**, 557–565.

73 R. R. Michelsen, S. F. M. Ashbourn and L. T. Iraci, *J. Geophys. Res.*, 2004, **109**, D23205.

74 P. E. Sorensen and W. P. Jencks, *J. Am. Chem. Soc.*, 1987, **109**, 4675–4690.

75 E. Maimon, A. Lerner, A. Samuni and S. Goldstein, *J. Phys. Chem. A*, 2018, **122**, 7006–7013.

76 A. S. Evans, A. D. Cohen, Z. A. Gurard-Levin, N. Kebede, T. C. Celius, A. P. Miceli and J. P. Toscano, *Can. J. Chem.*, 2011, **89**, 130–138.

77 Y. Izato, K. Shiota and A. Miyake, *Sci. Technol. Energ. Mater.*, 2019, **80**, 212–221.

78 K. Q. Zhang and S. T. Thynell, *J. Phys. Chem. A*, 2017, **121**, 4505–4516.

79 V. Shafirovich and S. V. Lymar, *Proc. Natl. Acad. Sci. U. S. A.*, 2002, **99**, 7340–7345.

80 I. Sanchez-Garcia, L. J. Bonales, H. Galan, J. M. Perlado and J. Cobos, *Radiat. Phys. Chem.*, 2021, **183**, 109402.

81 L. W. Chen, X. C. Li, J. Zhang, J. Y. Fang, Y. M. Huang, P. Wang and J. Ma, *Environ. Sci. Technol.*, 2015, **49**, 10373–10379.

82 M. Simic and E. Hayon, *J. Am. Chem. Soc.*, 1971, **93**, 5982–5986.

83 P. Neta, P. Maruthamuthu, P. M. Carton and R. W. Fessenden, *J. Phys. Chem.*, 1978, **82**, 1875–1878.

84 M. Lefort and X. Tarrago, *J. Inorg. Nucl. Chem.*, 1961, **16**, 169–186.

85 D. Behar, D. Shapira and A. Treinin, *J. Phys. Chem.*, 1972, **76**, 180–186.

86 R. Musat, J. L. Marignier, C. Le Naour, S. Denisov, L. Venault, P. Moisy and M. Mostafavi, *Phys. Chem. Chem. Phys.*, 2020, **22**, 5188–5197.

87 J. Lind and G. Merenyi, *J. Phys. Chem. A*, 2006, **110**, 192–197.

88 N. Karpel Vel Leitner, P. Berger, G. Dutois and B. Legube, *J. Photochem. Photobiol., A*, 1999, **129**, 105–110.

89 A. J. Elliot, *Radiat. Phys. Chem.*, 1989, **34**, 753–758.

90 G. P. Horne, T. S. Grimes, B. J. Mincher and S. P. Mezyk, *J. Phys. Chem. B*, 2016, **120**, 12643–12649.

91 G. P. Horne, T. S. Grimes, W. F. Bauer, C. J. Dares, S. M. Pimblott, S. P. Mezyk and B. J. Mincher, *Inorg. Chem.*, 2019, **58**, 8551–8559.

92 G. P. Horne, A. Wilden, S. P. Mezyk, L. Twight, M. Hupert, A. Stark, W. Verboom, B. J. Mincher and G. Modolo, *Dalton Trans.*, 2019, **48**, 17005–17013.